



HAL
open science

Circulation in Drake Passage revisited using new current time series and satellite altimetry: 2. The Ona Basin

Ramiro Ferrari, Christine Provost, Nathalie Sennéchaël, Jae Hak Lee

► To cite this version:

Ramiro Ferrari, Christine Provost, Nathalie Sennéchaël, Jae Hak Lee. Circulation in Drake Passage revisited using new current time series and satellite altimetry: 2. The Ona Basin. *Journal of Geophysical Research. Oceans*, 2013, 118 (1), pp.147-165. 10.1029/2012JC008193 . hal-01234139

HAL Id: hal-01234139

<https://hal.science/hal-01234139v1>

Submitted on 15 Oct 2021

HAL is a multi-disciplinary open access archive for the deposit and dissemination of scientific research documents, whether they are published or not. The documents may come from teaching and research institutions in France or abroad, or from public or private research centers.

L'archive ouverte pluridisciplinaire **HAL**, est destinée au dépôt et à la diffusion de documents scientifiques de niveau recherche, publiés ou non, émanant des établissements d'enseignement et de recherche français ou étrangers, des laboratoires publics ou privés.

Copyright

Circulation in Drake Passage revisited using new current time series and satellite altimetry: 2. The Ona Basin

Ramiro Ferrari,¹ Christine Provost,¹ Nathalie Sennéchaël,¹ and Jae-Hak Lee²

Received 9 May 2012; revised 23 November 2012; accepted 29 November 2012; published 25 January 2013.

[1] Time series of horizontal velocities were obtained at four mooring sites across the Ona Basin, southern Drake Passage, during 26 months (February 2006 to April 2008). The moorings were located under the Jason satellite ground-track #104, allowing precise comparisons with various other altimetry products. Velocities as high as 0.5 m s^{-1} at 500 m depth were observed during current pulses. Mean velocity amplitudes at 500 m reached 0.22 m s^{-1} at 58.5°S and 0.15 m s^{-1} at 60°S , but were smaller at 59°S and 60.5°S . Mean velocities at 2500 m depth varied between 0.05 and 0.10 m s^{-1} and were westward on two of the moorings, suggesting recirculation in the center of the basin. Mean velocities were consistent with a general cyclonic circulation in the Ona Basin. The mean velocity vectors were observed to rotate with depth, the sense of rotation depending upon mooring sites. Standard deviation ellipses were close to circular except on the continental slope (60.5°S) where they were stretched in the direction of isobaths. The southernmost mooring was under sea ice in winter, and velocity variations were reduced in amplitude during that period. The horizontal velocities were highly coherent in the vertical. Altimetrically derived surface geostrophic velocities compared well with the in situ velocities and were used to investigate further the flow over the West Scotia Ridge and in the center of the Ona Basin to the East of the highest part of the Shackleton Ridge, which provides some shelter from the eastward flowing Antarctic Circumpolar Current.

Citation: Ferrari, R., C. Provost, N. Sennéchaël, and J.-H. Lee, (2013), Circulation in Drake Passage revisited using new current time series and satellite altimetry: 2. The Ona Basin, *J. Geophys. Res. Oceans*, 118, 147–165, doi:10.1002/2012JC008193.

1. Introduction

[2] The Ona Basin (OB; 52°W – 62°W , 57°S – 61°S), southern Drake Passage, is bordered to the south by the South Scotia Ridge, to the north by the West Scotia Ridge (WSR), to the east by the Terror Rise and to the west by the Shackleton Fracture Zone (SFZ) (Figure 1b). The narrow, shallow, and long crest of the SFZ exerts a strong constraint on the Antarctic Circumpolar Current (ACC) and its three frontal systems. The two northernmost frontal systems of the ACC—the Subantarctic Front (SAF) and the Polar Front (PF)—veer to the north, with the SAF following more or less the continental slope of South America and the PF flowing over the West Scotia Ridge (Figure 1a) [Orsi *et al.*, 1995]. The southernmost frontal system of the ACC—the Southern ACC Front system (SACCF)—is strongly affected by the SFZ barrier as it proceeds eastwards. The SACCF branches can be detected using satellite altimetry [Sokolov and Rintoul, 2009; Barré *et al.*, 2011] and appear as local minima in chlorophyll-*a*

concentration in cloud-free summer ocean color images. An example is shown in Figure 2. The northern branch, the SACCF-N, loops to the north rejoining the PF at 59°S , where both these oceanographic features are steered eastward by the West Scotia Ridge; the southern branch, SACCF-S, enters the Ona Basin through the Shackleton Gap (60.7°S , 56.3°W) and overshoots northward forming a large meander (Figure 2). Altimetric data show that the recurrent meander of the SACCF-S breaks up into cyclonic eddies [Barré *et al.*, 2011; Provost *et al.*, 2011].

[3] Indeed, the circulation in the Ona Basin is marked by the presence of deep-reaching cyclonic and anticyclonic eddies revealed by hydrographic data [e.g., Cunningham *et al.*, 2003; Provost *et al.*, 2011], by Argo float data [Barré *et al.*, 2008], by ocean color and infrared imagery [Kahru *et al.*, 2007; Provost *et al.*, 2011], and by altimetric data [Barré *et al.*, 2011]. The transport of some of these full-depth eddies is as high as 35 Sv [Renault *et al.*, 2011]. An altimetry-based census of eddies in the Ona Basin revealed that, on average, two to three cyclonic eddies and two to four anticyclonic eddies are observed at any one time in the OB [Barré *et al.*, 2011]. Most of the anticyclonic eddies are observed to originate from a meander of the PF and SACCF-N over the Ona seafloor depression (OSD; Figure 1b) in the northwestern part of the Ona Basin [Barré *et al.*, 2008; 2011]. The meander overlying the OSD is an intermittent feature, which sheds anticyclonic westward-propagating deep-reaching eddies. Most of the anticyclonic eddies propagate westward until they reach the SFZ where they

¹LOCEAN, UMR 7159, CNRS/UPMC/MNHN/IRD, Université Pierre et Marie Curie, Paris, France.

²KORDI, Korean Ocean Research and Development Institute, Ansan, Seoul, Republic of Korea.

Corresponding author: R. Ferrari, LOCEAN, T 45-46, 5E, 4 place Jussieu, 75252 Paris cedex 05, France. (rfiod@locean-ipsl.upmc.fr)

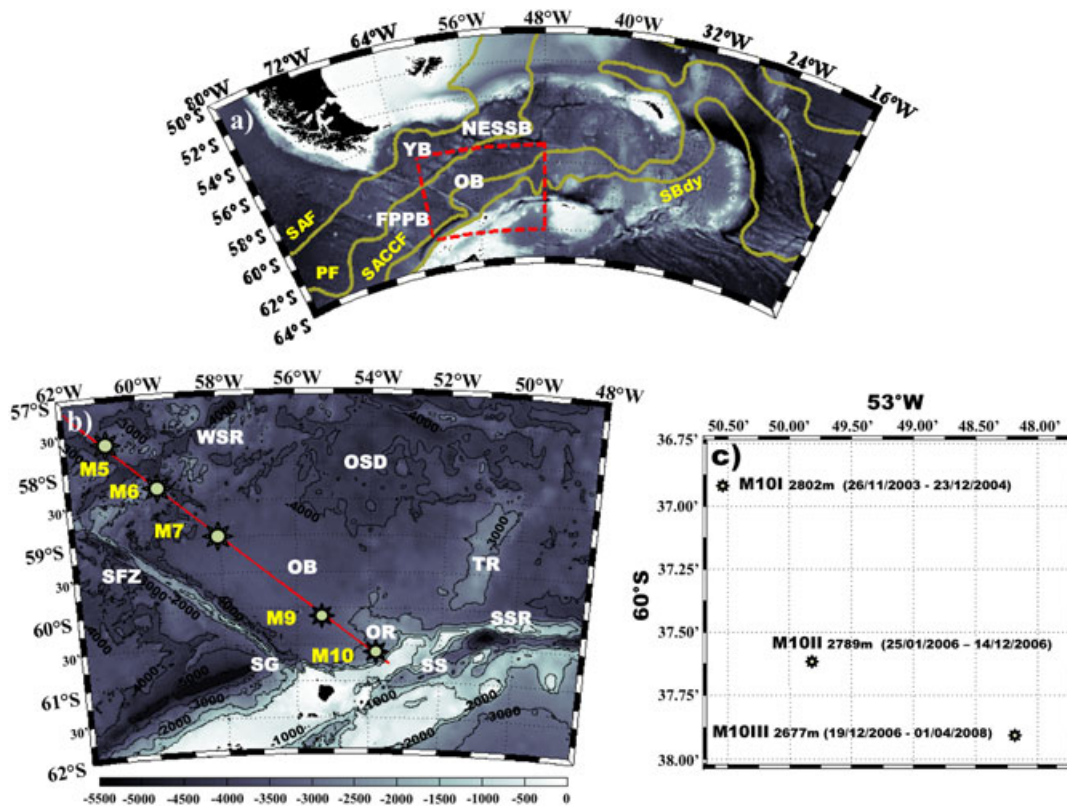


Figure 1. Bottom topography and locations of the current meter moorings. (a) Bottom topography of the Drake Passage with the main basins labeled: Yaghan Basin (YB), Ona Basin (OB), Former Phoenix Plate Basin (FPPB) and Northeast Scotia Sea Basin (NESSB). The yellow lines correspond to the mean location of the major fronts, according to *Orsi et al.* [1995], from north to south: SAF, Subantarctic Front; PF Polar Front; SACCF, South ACC Front and SBdy, southern boundary of the ACC. (b) Black stars indicate the locations of the moorings deployed along the Jason ground track #104 (red line) in the Ona Basin in January 2006. The Ona Basin is the semi-closed basin delimited (dotted red rectangle) by the Shackleton Fracture zone (SFZ), Shackleton Gap (SG), Shackleton Shelf (SS), West Scotia Ridge (WSR), South Scotia Ridge (SSR), Ona Seafloor Depression (OSD), Ona Rise (OR) and Terror Rise (TR). (c) Zoom on the sites of mooring M10. Bottom depth, deployment, and recovery dates are indicated.

dissipate. A few are observed to rejoin the PF and SACCF over the WSR. Cyclonic eddies are observed to form mainly in the southern part of the Ona Basin [*Provost et al.*, 2011].

[4] As summarized above, our understanding of the circulation in the Ona Basin comes from snapshots from hydrographic cruises, satellite data, and Argo floats. To our knowledge, the only existing in situ current time series come from a 14 month long mooring deployment on the continental slope (53.8°W and 60.6°S) shown in *Barré et al.* [2008].

[5] We reexamined the circulation in the Ona Basin using the first time series of velocity gathered in the center of the Ona Basin in conjunction with satellite altimetric data. The in situ data were obtained at four mooring sites located under the Jason satellite ground track #104 during 26 months (Figure 1b). They document the mean flow, variability, and vertical structure of the currents, as well as the predominant time scales during this period. They allowed us to assess the quality of the altimetric data and in return the altimetric data helped our understanding of the large-scale structure in which the point measurements are embedded. The 18 years of satellite measurements also provided a temporal context for the 2 year current meter time series.

This descriptive work is necessary before investigating the dynamics further.

[6] Data are presented in section 2. Basic statistics on the velocity measurements, vertical structure of the flow, and time scales are discussed in section 3. Surface velocities computed using different altimetric data sets are compared to the in situ data in section 4. Because altimetrically derived velocities perform well to the north of 60°S, they are used together with the in situ data to investigate the flow over the West Scotia Ridge and in the center of the Ona Basin out to the highest part of the SFZ (section 5). Finally, section 6 synthesizes the main results of this study and puts forward several perspectives.

2. Data

2.1. Current Meter Data

[7] An array of 10 moored current meters was deployed in January 2006 (20–25 January) across the Drake Passage from the R/V *Polarstern* (Alfred Wegener Institute, Bremerhaven). These moorings were located under the Jason satellite ground-track #104, parallel to the DRAKE 79 main line moored array [*Hofmann and Whitworth*, 1985] on the eastern side of the

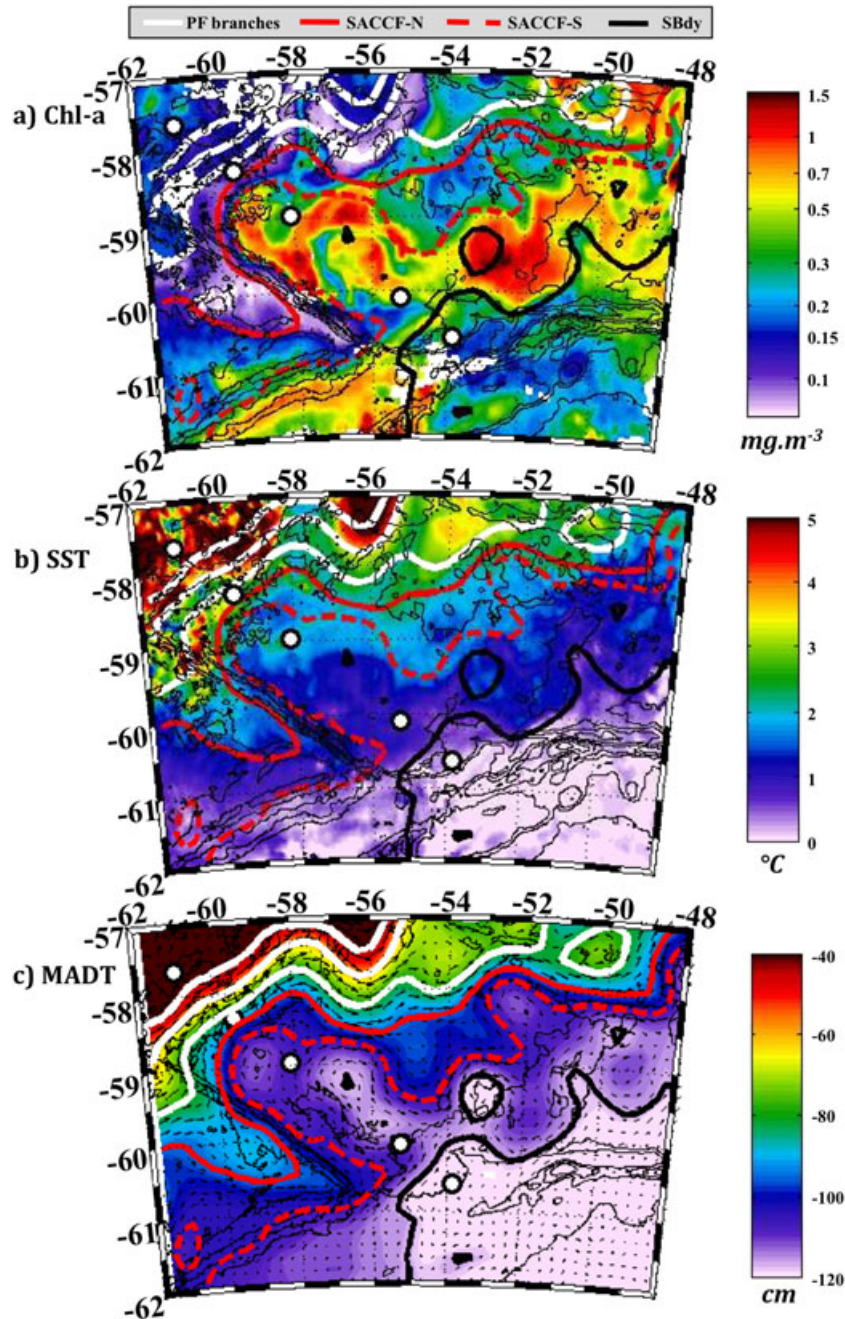


Figure 2. Satellite views of the Ona Basin. (a) Chlorophyll-*a* concentration (in $\text{mg}\cdot\text{m}^{-3}$) from ocean color MODIS image from 11 December 2006 (4 km resolution). (b) Sea surface temperature ($^{\circ}\text{C}$) from concomitant infrared image (MODIS, 4 km resolution). (c) Seven day composite absolute dynamic topography map (centimeters) centered on December 13. Locations of front branches and eddies are indicated. PF branches are represented by white isolines, SACCF branches by red isolines (northern branch SACCF-N solid line and southern branch SACCF-S dashed line) and SBdy front by a black isoline. Isobaths (1000, 2000, 3000, 4000, and 5000 m) and locations of the current meter moorings (white circles) are shown in all panels.

Shackleton Fracture Zone. The R/V *Polarstern* recovery cruise took place in March–April 2008. Two of the moorings (M2 and M8) could not be recovered. The five northernmost moorings, located in the Yaghan Basin, are presented in Ferrari *et al.* [part I, 2012]. Here we focus on the five southernmost moorings (M6 through M10) lined up in the Ona Basin (Figure 1b), and we make use of M5 data for the analysis of the flow over the West Scotia Ridge (section 5.1). M10 was retrieved after one year by the Korean Ocean Research and Development Institute

and redeployed. The first part is referred to as M10-II (25 January 2006 to 14 December 2006) and the second part, as M10-III (19 December 2006 to 12 March 2008) (Figure 1c). We also make use of the data from M10-I, a 14 month long mooring deployment (26 November 2003 to 23 December 2004) performed within the Korean Antarctic Research Program [Lee *et al.*, 2007] on the continental slope of the Antarctic Peninsula (60.6°S and 53.8°W). The location of M10-I is within 3 km of M10-II and M10-III (Figure 1c).

The M10-I data were presented in *Barré et al.* [2008]. All the moorings (M6, M7, M9, M10) were carrying three current meters at approximately 500, 1000, and 2500 m depths, and two moorings (M6 and M7) were equipped with microcats (Figure 3). M6, M7, M9, and M10 were placed at the cross-over point of Jason track #104 with tracks 111, 187, 85, and 161, respectively. The velocity records ended prematurely for two current meters on M7 (690 instead of 803 days) and leaks led to no data on one instrument on M10-II (at 500 m) and on M10-III (at 2500 m). The other current meters had full records (Table 1 and Figure 3). The reader is referred to the data report of *Kartavtseff* [2008] for further technical information on the instruments, data calibration, and magnetic corrections.

[8] Velocity-component data have been low-pass filtered, with a cutoff period of 25 h (in order to remove inertial and tidal variance) and then subsampled at a daily rate. Moorings were pulled up and down severely during strong current pulses over periods of several days. The standard deviation of the vertical displacement varied from 20 to 82 dbars for the upper instruments (Table 1). Largest displacements occurred at moorings M6 and M9; they reached or exceeded 350 m on two and six occasions, respectively. The method developed by *Hogg* [1986, 1991] and modified by *Cronin et al.* [1992] was used to correct the effects of mooring motion. Details of the correction method are presented in Appendix A of the companion paper [*Ferrari et al.*, part I, 2012]. The method did not work at M10 where temperature profile is unstable

[*Provost et al.*, 2011] and data at M10 were not corrected. In the following sections, daily-corrected velocities are used when available that is at M6, M7, and M9 (Figure 4).

2.2. Satellite Data

[9] 1. *Sea surface temperature and ocean color from MODIS.* A key feature of Aqua/MODIS is its capability to measure ocean surface color simultaneously with sea surface temperature. An important aspect is the need for image compositing because of the frequent cloud cover in the high latitudes of the study area. The 8 day composites and 4 km resolution standard mapped imagedata products are available through OceanColor FTP (<http://oceancolor.gsfc.nasa.gov>). These high-resolution images reveal a wealth of structures, with narrow fronts, eddies, vortices, and filaments (Figure 2).

[10] 2. *Sea surface height data.* Satellite altimetry has provided continuous data since October 1992. We used two types of altimetric products arising from the Archiving, Validation and Interpretation of Satellite Oceanographic Data (AVISO): along-track Jason data and gridded multisatellite products (<http://www.aviso.oceanobs.com>). We also used a regional along-track data set developed, validated, and distributed by the Centre de Topographie des Océans et de l'Hydrosphère/ Laboratoire d'Etudes en Géophysique et Océanographie Spatiales (CTOH/LEGOS) (<http://legos.obs-mip.fr/>).

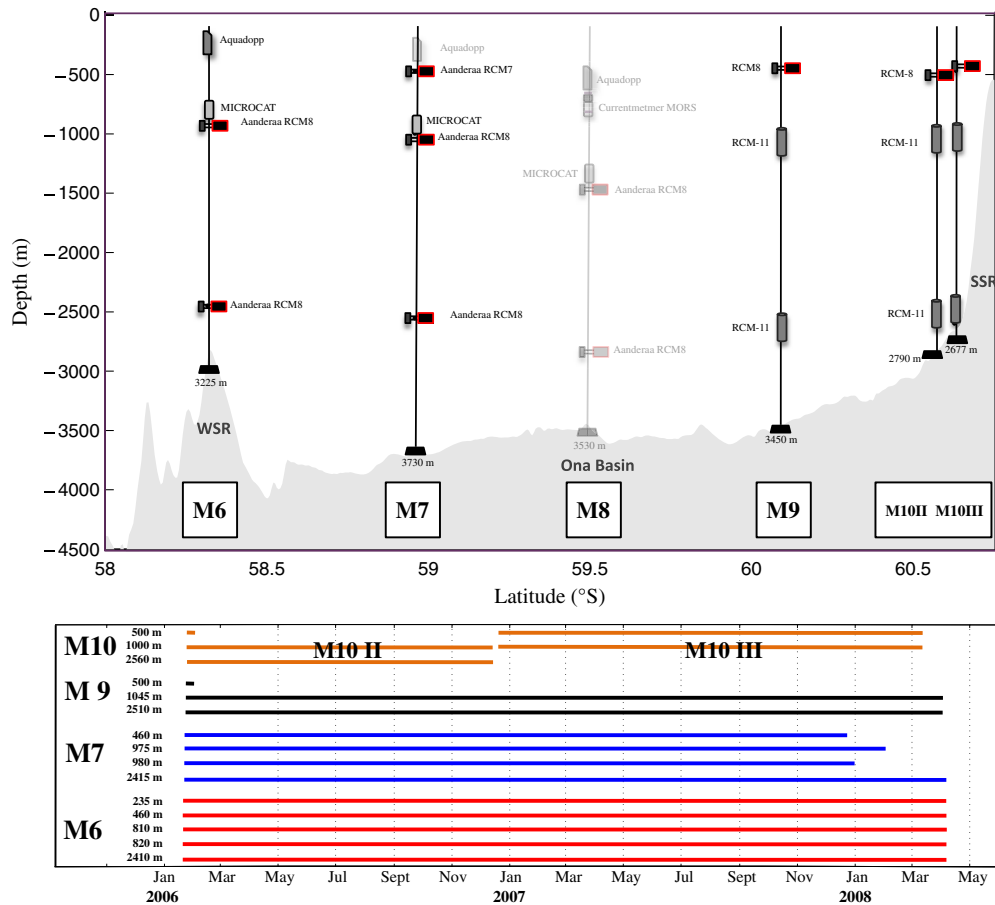


Figure 3. (top) Distribution of the mooring lines and instruments. Mooring M8 (half-toned) was lost. The South Scotia Ridge (SSR) and West Scotia Ridge (WSR) are labeled. (bottom) measurement calendar.

Table 1. Statistics of the Current Meter Measurements. P is the Mean Pressure Averaged Over the Record Length and σ_p Denotes the Standard Deviation. V is the Modulus of the Time Average of the Velocity, $\text{ang}(V)$ is the Mean Velocity Direction (Positive Values are Clockwise) and V_{max} the Maximum of the Velocity Modulus. The Last Three Columns Represent the Parameters of Standard Deviation Ellipses. Positive Values of the Angles ($\text{ang}(V)$ and Major Axis Direction) are Clockwise and Relative to the Geographical North. Velocity Data Were Corrected to Remove the Mooring Motion Effects Except M10

| Mooring | Days | P (dbar) | σ_p (dbar) | V (cm s^{-1}) | $\text{ang}(V)$ (deg) | V_{max} (cm s^{-1}) | Major Axis (cm s^{-1}) | Minor Axis (cm s^{-1}) | Major Axis Direction (deg) |
|---------|------|------------|-------------------|----------------------------|-----------------------|---|-----------------------------------|-----------------------------------|----------------------------|
| M6 | 805 | 237 | 64 | 21.5 | 43 | 74.8 | 14.4 | 11.9 | 7 |
| | 805 | 828 | 70 | 13.5 | 38 | 50.9 | 8.3 | 6.3 | 1 |
| | 805 | 2449 | 11 | 5.7 | 18 | 29.2 | 5.3 | 3.7 | -25 |
| M7 | 690 | 467 | 15 | 0.7 | 105 | 28.8 | 7.2 | 6.2 | 26 |
| | 690 | 991 | 13 | 2.2 | 187 | 24.3 | 6.2 | 5.6 | 10 |
| | 803 | 2553 | 23 | 3.9 | 202 | 35.7 | 6.4 | 5.8 | 21 |
| M9 | 800 | 1057 | 82 | 10.2 | 325 | 50.5 | 10.6 | 8.6 | 11 |
| | 800 | 2560 | 32 | 8.7 | 312 | 41.5 | 9.0 | 8.2 | -6 |
| M10I | 394 | 514 | 61 | 2.8 | 102 | 41.2 | 12.5 | 6.8 | 41 |
| | 394 | 1003 | 56 | 2.6 | 116 | 28.7 | 10.8 | 5.5 | 40 |
| | 394 | 2595 | 6 | 4.0 | 157 | 33.8 | 8.8 | 4.8 | 41 |
| M10II | 337 | 1068 | 21 | 1.4 | 140 | 27.5 | 7.3 | 4.8 | 44 |
| | 324 | 2598 | 1 | 3.8 | 166 | 22.2 | 6.1 | 3.9 | 32 |
| M10III | 438 | 466 | 20 | 2.4 | 55 | 39.6 | 8.6 | 4.6 | 43 |
| | 437 | 979 | 17 | 2.2 | 64 | 33.0 | 7.5 | 4.5 | 44 |

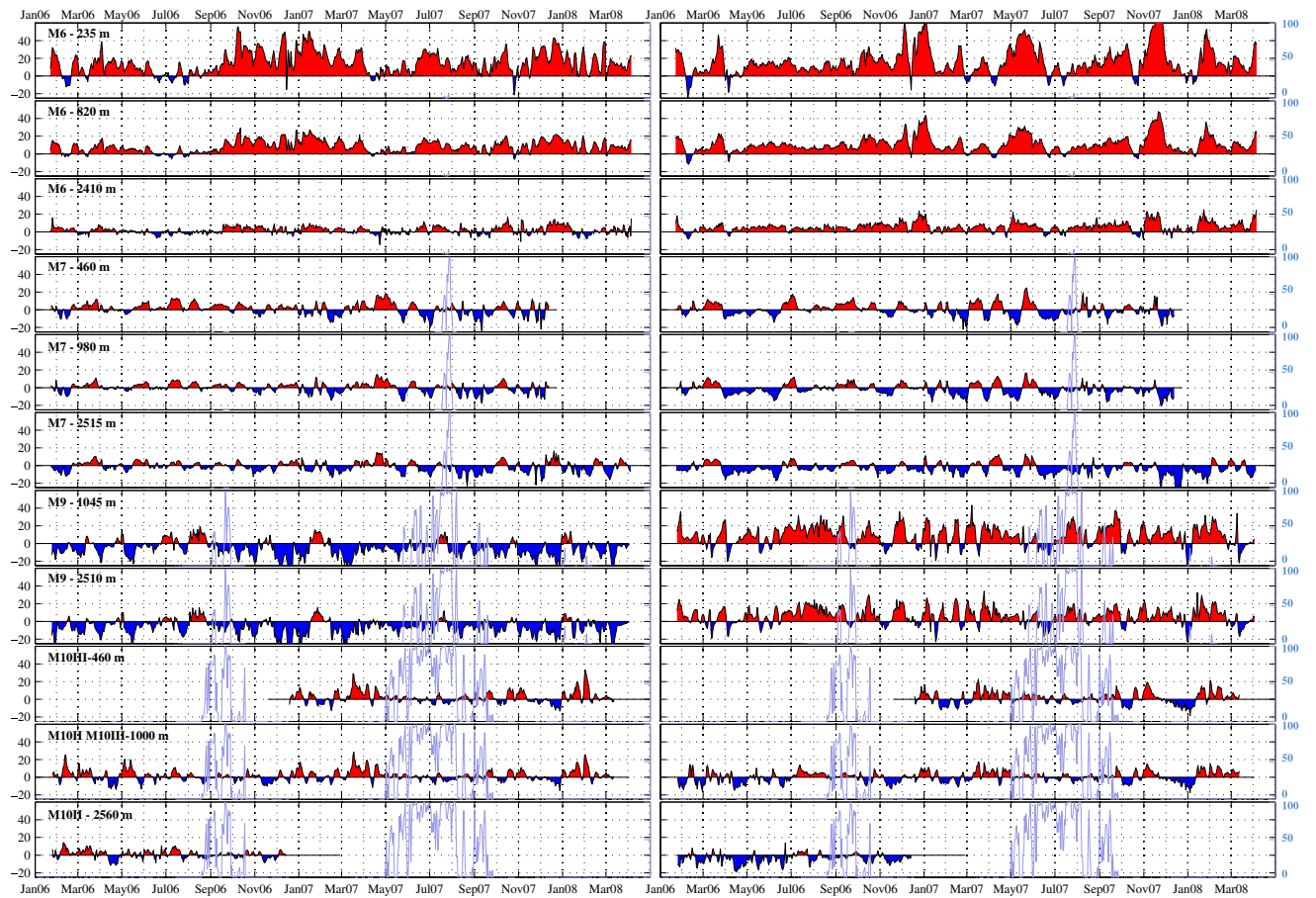


Figure 4. Time series of velocities (in cm s^{-1}) from January 2006 to April 2008. (left) The zonal component and (right) the meridional component. Positive velocities are shaded in red, and negative velocities are shaded in blue. All data are low-pass-filtered with a resampling interval of 24 h. Velocity data (except those for M 10) were corrected for vertical mooring motions. Light blue times series indicate sea-ice concentration (%).

[11] The along-track product from AVISO consists of sea-level anomaly (SLA) and absolute dynamic topography, which is the sum of SLA and a mean dynamic topography value (MDT). Like *Barré et al.* [2011], we used the CNES-CLS09 MDT [*Rio et al.*, 2009]. Jason-1 was launched on 7 December 2001 and repeats its orbital cycle every 9.9156 days. The along-track data processing was described by *Ducet et al.* [2000]: the raw along-track SLA data, sampled every 6.2 km, were filtered to reduce measurement noise, using a linear Lanczos low-pass filter with a cutoff at 70 km at latitudes higher than 50°S and subsampled every 18.5 km in the Drake Passage.

[12] The multisatellite gridded products consist of SLA maps with a spatial resolution of $1/3^\circ \times 1/3^\circ$ on a Mercator grid (about 18.5 km resolution in the Ona Basin) at 7 days and 1 day intervals. They are produced by merging altimetric observations from several satellites (when available): TOPEX/Poseidon or Jason-1, 2; ERS satellite (ERS-1/2); Environmental Satellite (Envisat); and Geosat Follow-on (GFO) [*Ducet et al.*, 2000]. We used weekly and daily maps of mean absolute dynamic topography (MADT) (the sum of sea level anomalies and the CNES-CLS09 MDT). They were used to locate frontal branches, major eddies, as in *Barré et al.* [2011], and to produce maps of surface geostrophic velocities.

[13] Close to the coast, altimeter observations are often of lower quality, for a number of reasons, such as land contamination of the satellite footprints or inaccurate resolution of the corrections of the high-frequency ocean response to tidal and atmospheric loading. The CTOH computes and distributes along-track sea level anomalies (SLA) that are produced using a specific reprocessing designed to improve both the quantity and quality of SLA estimates in coastal regions. The method is detailed in *Roblou et al.* [2007].

[14] 3. *Sea-ice data.* Southern Drake Passage is occasionally covered with sea ice in winter. We used sea-ice concentration data provided by the Institute of Oceanography of the University of Hamburg (<http://www.ifm.zmaw.de/forschung/fernerkundung-assimilation/meereis/amr-e-ice-concentration/>). The daily products have a spatial resolution of 6.25 km and were calculated with the ARTIST (Arctic Radiation and Turbulence Interaction Study) sea-ice concentration algorithm using AMSR-E 89-GHz brightness temperatures [*Spreen et al.*, 2008]. Sea-ice concentration is defined as the coverage of a unit area with sea ice. It can be expressed either by values or as a percentage of the unit area: 0% means the area is totally covered by open water and 100% means that the area is totally covered by sea ice. The sea-ice extent is the cumulative area covered with sea ice inside a specifically selected ice-concentration boundary (15%). An extreme sea-ice cover event reached as far north as M7 during three weeks in 2007, from mid-July to early August (Figure 4). M9 was sea-ice covered during two periods (September 2006 and for 16 weeks from late June to mid-September 2007) (Figure 4). The M10 location was sea-ice covered during three months in 2004 (from March to June), two months in 2006 (from mid-August to mid-October) and four and a half months in 2007 (from May to mid-September) (Figure 4).

www.ifm.zmaw.de/forschung/fernerkundung-assimilation/meereis/amr-e-ice-concentration). The daily products have a spatial resolution of 6.25 km and were calculated with the ARTIST (Arctic Radiation and Turbulence Interaction Study) sea-ice concentration algorithm using AMSR-E 89-GHz brightness temperatures [*Spreen et al.*, 2008]. Sea-ice concentration is defined as the coverage of a unit area with sea ice. It can be expressed either by values or as a percentage of the unit area: 0% means the area is totally covered by open water and 100% means that the area is totally covered by sea ice. The sea-ice extent is the cumulative area covered with sea ice inside a specifically selected ice-concentration boundary (15%). An extreme sea-ice cover event reached as far north as M7 during three weeks in 2007, from mid-July to early August (Figure 4). M9 was sea-ice covered during two periods (September 2006 and for 16 weeks from late June to mid-September 2007) (Figure 4). The M10 location was sea-ice covered during three months in 2004 (from March to June), two months in 2006 (from mid-August to mid-October) and four and a half months in 2007 (from May to mid-September) (Figure 4).

3. Current Meter Observations

3.1. Current Meter Statistics

[15] Velocity time series from January 2006 to April 2008 are shown in Figure 4. M10-I data from December 2003 to December 2004 are shown in *Barré et al.* [2008] (their Figure 6). Basic statistics from all mooring data are summarized in Table 1. The statistics are attributed to the mean depth of the instruments. At each mooring, the measurements showed a vertical consistency of the velocities. The standard deviation ellipse axes and mean velocity vectors were roughly parallel at the three levels for all moorings (Figure 5 and Table 1). However, a small rotation of the mean velocity vector suggested an upwelling or

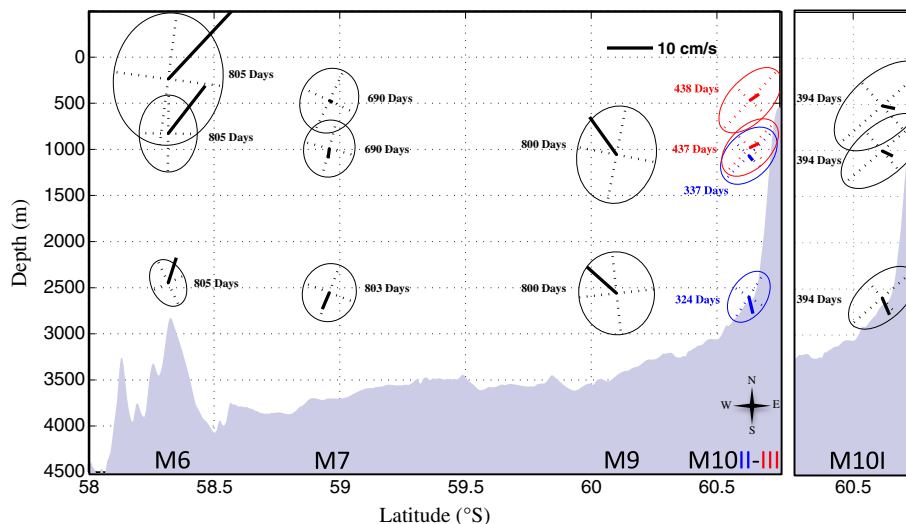


Figure 5. Mean velocity and velocity standard deviation ellipses for each current meter. The number of data days is indicated.

downwelling at the mooring location, depending on the sense of rotation: clockwise rotation from the upper vector to the deeper vector for upwelling, and counterclockwise for downwelling (Appendix A). Estimates of vertical velocities have high uncertainties, which are quantified in Appendix A (Table A1).

[16] 1. *Northern Ona Basin*. M6 is located on the WSR over the 3220 m isobath (Figure 1). Remarkable features are the strong eastward component, marked variability, and coherence between the measured horizontal flow at different vertical levels (Figure 4 and Table 2). Maximum velocities reached 0.75 m s^{-1} at 235 m depth and 0.50 m s^{-1} at 820 m (November 2007) (Table 1 and Figure 4). Westward flows were noticed, during short periods (< 10 days), on seven occasions, with amplitudes less than 0.20 m s^{-1} .

[17] The major axis of the standard deviation ellipses of the two upper levels was oriented from north to south, while that of the deeper level was stretched out and rotated from southeastward to northwestward (Figure 5). Mean velocities at M6 were larger than the ellipse axes. The mean velocity amplitude was 0.22 m s^{-1} at 235 m and decreased with depth to reach values of 0.06 m s^{-1} at 2410 m depth. The counterclockwise rotation of the mean velocity vector with depth (Figure 5) suggests a mean downwelling through the water column estimated to be on the order of 10 m day^{-1} (Appendix A).

[18] 2. *Central Ona Basin*. M7 is located at 59°S , in the center of the Ona Basin; it presented a flow highly correlated in the vertical and with a large variability in both direction and strength (Figure 4 and Table 2). The maximum velocity amplitude recorded at M7 was 0.35 m s^{-1} at 2500 m depth in December 2007 after the two upper current meters had stopped recording. The December 2007 event is discussed in section 5. The mean velocities were small, increasing with depth and reaching values of 0.04 m s^{-1} at 2515 m. The clockwise rotation of the mean velocity vector suggests a mean upwelling through the water column. The mean vertical velocity estimates were a few meters per day (Appendix A). The standard deviation ellipses, close to circular, have axes larger than the mean velocities (Figure 5 and Table 1).

[19] M9 is the other mooring in the center of the Ona Basin. Velocity amplitudes there reached up to 0.50 and 0.40 m s^{-1} at 1045 and 2510 m, respectively, while the mean velocity amplitude at 1045 m was 0.10 m s^{-1} and 0.09 m s^{-1} at 2510 m (Table 1). The northward component was almost always positive, and southward flows during short periods (< 10 days) were observed on seven occasions. The standard deviation ellipses are close to circular, with

amplitudes comparable to the mean velocity values (Table 1 and Figure 5). The counterclockwise rotation of the mean velocity vector with depth (Figure 5) suggests a mean downwelling below 1000 dbar. The mean vertical velocity estimate between the two lower current meters was about 15 m day^{-1} .

[20] 3. *Southern Ona Basin*. M10 is located on the continental slope over the 2700 m isobath. The time series from M10-I, presented in *Barré et al.* [2008], comprises 14 month long current meter data from November 2003 to December 2004. The mean velocities were small, less than 0.05 m s^{-1} , with an eastward-southeastward component at all depths (Table 1 and Figure 5). M10-II and M10-III are presented in Figure 4. At M10-II (February–December 2006) mean velocities were small, less than 0.04 m s^{-1} , to the southeast, increasing with depth, and consistent with the M10-I mean velocities. At M10-III (December 2006 to April 2008), mean velocities were less than 0.03 m s^{-1} and to the northeast at all depths. The velocity standard deviation ellipses are stretched in the direction of the isobaths (Figure 5). In all cases (M10-I, M10-II, and M10-III), velocity amplitudes were greater in summer than in winter (Figure 4). At M10-II and M10-III, velocity amplitudes were reduced when sea ice was present. The consistent clockwise rotation of the mean velocity vector with depth suggests a mean upwelling through the water column, which was estimated to be 1 m day^{-1} between 500 and 1000 m and $2\text{--}4 \text{ m day}^{-1}$ between 1000 and 2500 m (Appendix A). Coherence between the measured horizontal flow at different vertical levels is large (Figure 4 and Table 2).

[21] In summary, the mean velocities at the mooring sites are consistent with a mean cyclonic circulation in the Ona Basin, as described by *Barré et al.* [2008] and *Provost et al.* [2011]. Mean velocities were larger than their standard deviation at two mooring sites: at mooring M6, which recorded the strong eastward flow associated with the PF and SACCF-N over the WSR, and at mooring M9, which sampled a northwestward flow associated with the SACCF-S branch. Mean velocities at M7 and M10 are very small except at the deeper level where they are consistent with the mean cyclonic circulation in the Ona Basin. At the upper levels variations are large in both direction and amplitude. Velocity standard deviation ellipses were close to circular in the central Ona Basin and stretched in the direction of isobaths over the continental slope (60.5°S). The sea-ice cover in winter reduces velocity amplitudes at M10. A mean downwelling is indicated by a counter clockwise rotation of the mean velocity vectors at M6 and M9 and upwelling at M7 and M10.

Table 2. Correlation Coefficient (r) Between Time Series at Different Depths at Each Mooring. u Is the Zonal Velocity Component, v the Meridional Velocity Component and $|V|$ Is the Modulus of the Velocity. All Correlation Coefficients Are Above the 99% Confidence Limit Interval (the Highest Threshold for 99% CL Being $r=0.44$)

| Mooring | M6 | | M7 | | M9 | | M10 | |
|--------------------------------|---------|----------|---------|----------|-----------|----------|-----------|--|
| Depth (in meters) | 237/828 | 828/2449 | 467/991 | 991/2553 | 1057/2560 | 500/1000 | 1000/2500 | |
| u (in cm s^{-1}) | 0.95 | 0.66 | 0.93 | 0.89 | 0.88 | 0.96 | 0.69 | |
| v (in cm s^{-1}) | 0.97 | 0.73 | 0.93 | 0.86 | 0.89 | 0.94 | 0.66 | |
| $ V $ (in cm s^{-1}) | 0.95 | 0.62 | 0.82 | 0.70 | 0.79 | 0.91 | 0.61 | |

3.2. Empirical Orthogonal Functions Analysis of the Vertical Velocity Structure

[22] A principal component analysis was performed on non-normalized velocity anomalies, considering each mooring separately, to examine the vertical structure of the flow. The three leading empirical orthogonal functions (EOF) explained between 94 and 99% of the total variance, with the first EOF (EOF 1) explaining between 52.6 and 78.3% (Figure 6). EOF 1 at M6 was surface-intensified and we noted a slight counterclockwise rotation in direction below 1000 m (Figure 6). At M7, M9, and M10, the first EOF reflected the same vertical structure of the velocity field, with a consistent orientation and a slight decrease in amplitude with depth. At M10 EOF1 was consistently oriented in the direction of the isobaths.

[23] The second modes (EOF 2) accounted for a smaller fraction of the variance (between 17 and 39.1%) and have a structure reminiscent of, though complementary to, leading EOFs. We again noted a remarkable self-similarity in direction at all depths and a surface intensification, which was particularly important at M6.

[24] The third modes (EOF 3) explained less than 5.5% of the total variance. EOF3 were baroclinic showing opposite direction at the upper and lower levels and were bottom-intensified. At M10-II and M10-III, where only two levels were sampled (upper layer at M109-III and lower layer at M10-II), EOF 3 accounted for 9% and only 1.7%, respectively.

[25] Wavelet power spectra of the principal component time series associated with the EOFs were computed (not shown) and peaks over the 95% confidence level are reported. At M6, the principal components showed significant energy over a broad range of periods shorter than 80 days for EOF 1 and 32 days for EOF 2. The energy was mainly concentrated from

November 2006 to April 2007 (period bands of 16–50 days for EOF 1 and 10–32 days for EOF 2) and from September 2007 to March 2008 (period bands of 30–80 days for EOF 1 and 10–20 days for EOF 2). At M7, velocity fluctuations were more energetic in 2007 than in 2006. The most energetic period lasted from January 2007 to mid-August 2007, with energetic-period bands of 16–64 days for EOF 1 and 10–50 days for EOF 2. At M9, two periods with significant energy were observed for EOF 1: one, between 18 and 32 days, throughout the time series, and the second, between 32 and 64 days, from October 2006 to January 2007. The wavelet power spectra corresponding to EOFs 1 and 2 at M10 reflected the reduced velocity variation in the presence of sea-ice cover: with broad-band energy (10–90 days) during summer and no significant period of variability in winter.

4. Satellite-Derived Surface Geostrophic Velocities at the Mooring Sites

[26] The purpose of this section is to compare surface geostrophic velocities (SGV) computed from two different altimetric products with the in situ velocities at the level of the upper current meter (236 m at M6, 460 m at M7, 1045 m at M9, and 500 m at M10). SGVs were computed from maps of absolute dynamic topography (MADT) with a 7 day time resolution and from 10 day repeat Jason-1 track data. As moorings were located at crossover points of Jason-1 tracks, across-track velocities were computed from track 104 data and along-track 104 velocities from tracks 111, 187, 85, and 161 for M6, M7, M9, and M10, respectively (Figure 7). These intersecting tracks are temporally separated by 6 h at M6, 3 days at M7, 19 h at M9, and 2 days at M10. The angle between track 104 and intersecting tracks increases southward: 98.4° at M6, 101.1° at M7, 106.6° at M9, and 109.4° at M10.

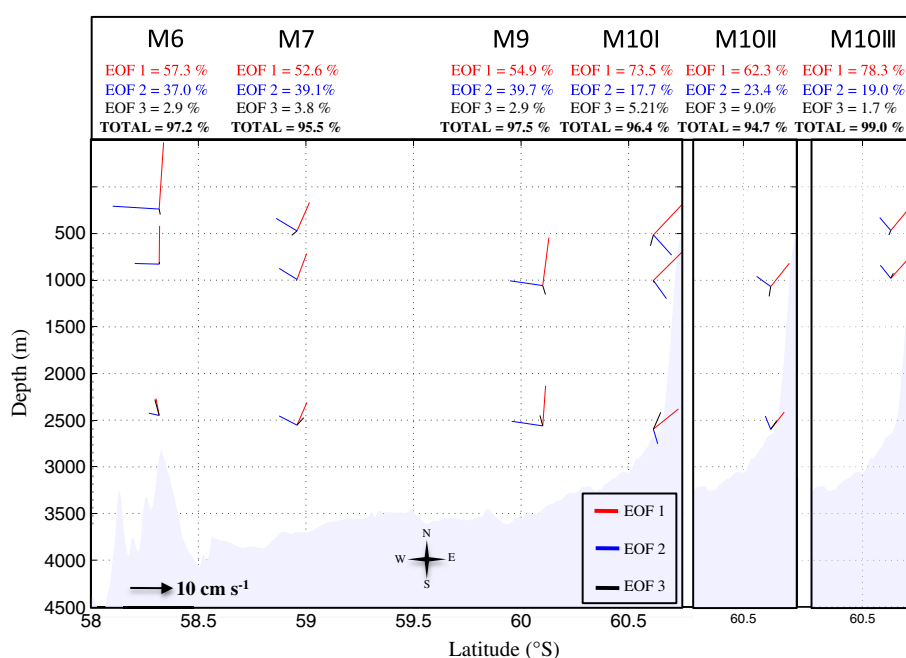


Figure 6. Empirical orthogonal functions (EOFs) at the different moorings with the percentage of variance explained by each mode. The red, blue, and black solid lines represent the first, second and third mode, respectively.

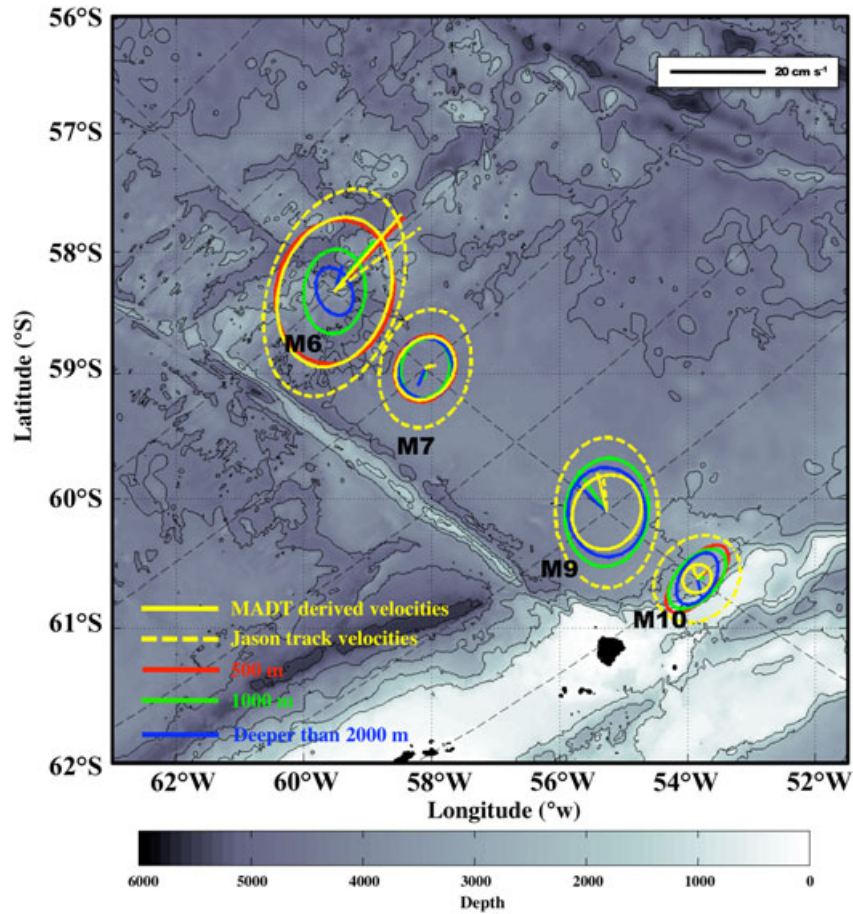


Figure 7. Mean and standard deviation ellipses of the altimetrically derived surface velocities and the in situ velocities over the sampling period. Surface velocities derived from MADT are shown by solid yellow lines and those derived from Jason-1 track data by dashed yellow lines. Standard deviation ellipses and mean of the in situ velocities are plotted in red for 500 m depth, green for 1000 m depth and blue for 2500 m. Time resolution is one day for in situ velocities, 7 days for MADT-derived velocities and 10 days for Jason-1 track-derived velocities. Black dotted lines crossing track 104 correspond to Jason ground-tracks # 111, 187, 85, and 161 (from north to south).

4.1. Means and Standard Deviation Ellipses

[27] Mean surface geostrophic velocities deduced from MADT and Jason-1 track data were calculated over the sampling period of the upper current meter at each mooring location and are reported in Table 3. Mean surface velocity amplitudes derived from MADT were comparable to the upper current meter velocity means at M6, M7 and M10 (difference less than 0.2 cm s^{-1} at M6 and M10 and about 0.8 cm s^{-1} at M7) and underestimated by 2 cm s^{-1} at M9 location (Table 3 and Figure 7). The directions of the mean surface velocities derived from MADT were similar to mean in situ surface velocity directions at M6 (no difference), at M9 and M10 (difference less than 20°) and were different by 51° at the M7 location where the mean velocity was small ($\approx 1 \text{ cm s}^{-1}$). Differences between mean surface velocity derived from Jason along-track data and mean in situ velocity were slightly larger, both in amplitude (2.2 cm s^{-1} at M6, 0.4 cm s^{-1} at M7, 2 cm s^{-1} at M9, and 1 cm s^{-1} at M10) and direction (3° at M6, 40° at M9, 60° at M7, and 160° at M10) (Table 3).

[28] Standard deviations computed from MADT surface geostrophic velocities were similar to in situ velocity variances at the two northernmost moorings (235 m at M6 and 460 m at M7) and smaller than in situ velocity standard deviations at the two southernmost moorings (Figure 7). The major axes of the standard deviation ellipses computed using the MADT data reached 8.0 cm s^{-1} (M9 location) and 3.2 cm s^{-1} (M10 location), whereas they were 10.6 cm s^{-1} and 7.3 cm s^{-1} for in situ velocities at 1045 m depth (M9) and 500 m depth (M10), respectively (Table 3). In contrast, the major axes of the standard deviation ellipses computed using the Jason-1 along-track data were more than 5 cm s^{-1} greater than the major axes of the standard deviation ellipses for in situ velocities (except at M10 where the track-data major axis is only 2.4 cm s^{-1} greater than the in situ major axis) (Table 3).

[29] In summary, surface velocities derived from maps of absolute dynamic topography every 7 days provide means that are in remarkable agreement with the mean in situ velocities recorded at the upper level on the moorings.

Table 3. Statistics of Altimetrically Derived Surface Geostrophic Velocities and Upper Current Meter Measurements. Mean Surface Velocities Derived From MADT (Gridded) and Jason Track 104 (Along Track) From AVISO Were Calculated Over the Sampling Period of the Upper Current Meter at Each Mooring Location. In the Table, V is the Modulus of the Time-Average of the Velocity and $\text{ang}(V)$ is the Angle the Mean Velocity Direction. Major Axis and Minor Axis Are the Lengths of the Standard Deviation Ellipse Axes. POSITIVE Values of the Angle of the Mean Velocity Direction ($\text{ang}(V)$) Are Clockwise and Relative to the Geographical North.

| Mooring (Jason-1 Tracks Intersections) | Angle Between Jason-1 Ground Tracks (°) | Distance Jason Track Intersection – Mooring Locations (m) | V (cm s ⁻¹) | | | Ang(V) (deg) | | | Major Axis (cm s ⁻¹) | | | Minor Axis (cm s ⁻¹) | | | |
|--|---|---|-------------------------|-----|--------------|-------------------------------|-----|----------------|----------------------------------|---------|------|----------------------------------|-------------------------------|---------|------|
| | | | In Situ (Depths) | | MADT Gridded | Jason Track 104 – Along Track | | MADT (Gridded) | Jason Track 104 (Along Track) | In Situ | | MADT (Gridded) | Jason Track 104 (Along Track) | In Situ | |
| | | | | | | | | | | | | | | | |
| M6 (104/111) | 98.4 | 293 | 21.52 (235 m) | 2.2 | 21.6 | 23.7 | 43 | 43 | 40 | 14.4 | 15.7 | 22.0 | 11.9 | 11.2 | 13.7 |
| M7 (104/187) | 101.1 | 950 | 0.71 (460 m) | 1.5 | 1.5 | 0.3 | 54 | 54 | 36 | 7.2 | 7.0 | 12.9 | 6.2 | 5.2 | 9.4 |
| M9 (104/85) | 106.6 | 614 | 10.24 (1045 m) | 8.1 | 8.1 | 8.3 | 346 | 346 | 2 | 10.6 | 8.0 | 15.8 | 8.6 | 6.9 | 11.0 |
| M10 (104/161) | 109.4 | 1270 | 2.05 (500 m) | 2.2 | 2.2 | 1.0 | 39 | 39 | 254 | 7.3 | 3.2 | 9.7 | 3.8 | 2.8 | 7.8 |

MADT-derived velocities provided a reasonable estimate of the velocity variance at the northern two moorings, an underestimation at M9 and missed the variability at M10. One should keep in mind that the upper-level data at M9 were from 1045 m depth. The velocity variance estimated by the Jason along-track data was larger than the in situ data variance at all moorings. We pursue these comparisons by examining time series of across-track velocities.

4.2. Time Series of Across-track Velocities

[30] Three time series of across-track velocities were produced: one from the upper-level in situ velocity and two from altimetry, one from the mapped product, the other from the along-track data (Figure 8).

[31] Correlations between in situ velocities and surface velocities derived from altimetric data were high and significant at the 99% confidence level, except for M10 (always below 0.5; not shown). Correlations of in situ velocities with surface velocities derived from weekly MADT ranged from 0.89 at M6 to 0.76 at M9, while correlations between in situ velocities and surface velocities derived from the Jason track #104 data reached 0.91 at M6 and decreased to 0.7 at M9 (at 1045 m) (Figures 8a, 8b, and 8c). Because the correlations were poor at M10, we examined velocities from the regional altimetry dataset (along-track Jason) developed by CTOH (see section 2). Correlation between in situ velocities and cross-track velocities derived from the CTOH product improved to 0.6 at M10-I (period 2003–2004) and 0.68 at M10-III (Figures 8d and 8f). However, to the north of 60°S, the CTOH product was too noisy and correlation with in situ velocity decreased.

[32] The time series comparison illustrated how the quality of the SLA track data degrades southward. Indeed, geophysical corrections applied to SLA measurements such as the wet tropospheric correction or the ocean tide corrections are degraded in high-latitude regions. Furthermore, the presence of sea ice in the south leads to the absence of data. The time series comparison also showed how the multisatellite gridded data provided better results.

[33] In conclusion, the multisatellite gridded maps of absolute dynamic topography, available every 7 days, provided surface geostrophic velocities that were in satisfactory agreement with the in situ velocities at M6 and M7 at 500 m depth (means, standard deviations, correlations). At M9, geostrophic velocities derived from MADT, although underestimated in amplitude, satisfactorily described the temporal variations of the in situ velocity. At M10, correlations between in situ and MADT-derived across-track velocities were poor. Improved results were obtained at M10 when using the CTOH altimetry product which is optimized for coastal waters.

[34] As the SGVs produced from MADT compared well with in situ velocities, we used the mapped surface geostrophic velocities to examine the surface two-dimensional flow field and gained further insight into the mooring measurements.

5. Interpretation of the Current Meter Data in the Light of Altimetry

[35] Altimetry provides both a spatial and temporal context (18 years) to the 2 year long point in situ measurements.

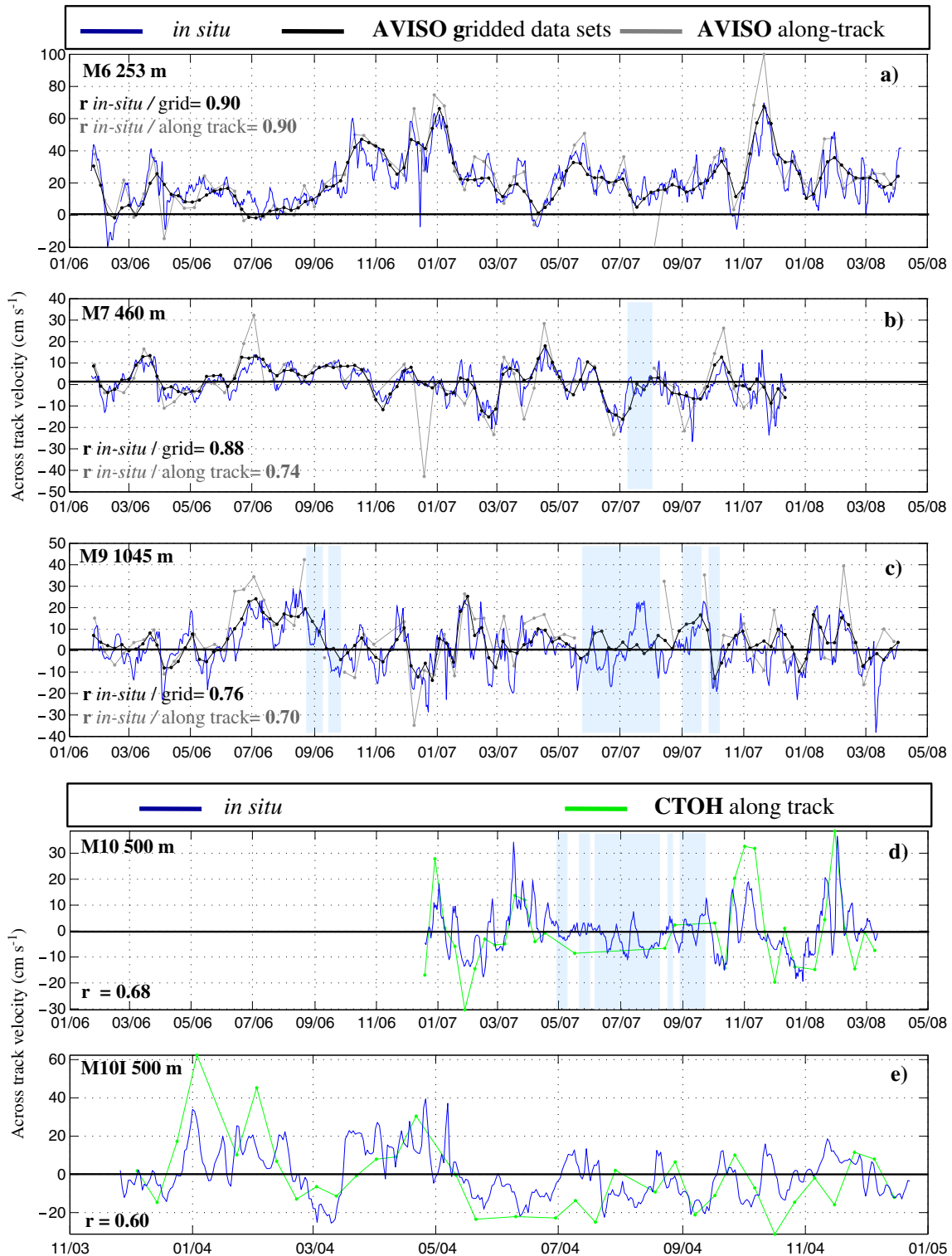


Figure 8. Correlation between the across-track component of the surface velocities derived from altimetry (in black and gray) and from the in situ velocity (blue) at the upper current meter level from January 2006 to April 2008. The surface velocities shown in black were computed from maps of absolute dynamic topography with a 7 day resolution. The surface velocities shown in gray were computed from the along-track data (track 104) with a 10 day resolution. (a) M6, (b) M7, and (c) M9. (d and e) For M10, CTOH altimetric data along Jason track 104 were used and are shown in green. The light blue areas correspond to periods of ice cover.

We first examined cross-track component of the mapped surface geostrophic velocities along Jason tracks 28 and 104 to provide a spatial background for the in situ measurements

(Figure 9a). Track 28 is upstream from track 104 and its southern part happens to be located over the crest of the Shackleton transverse ridge at the entrance to the Ona Basin.

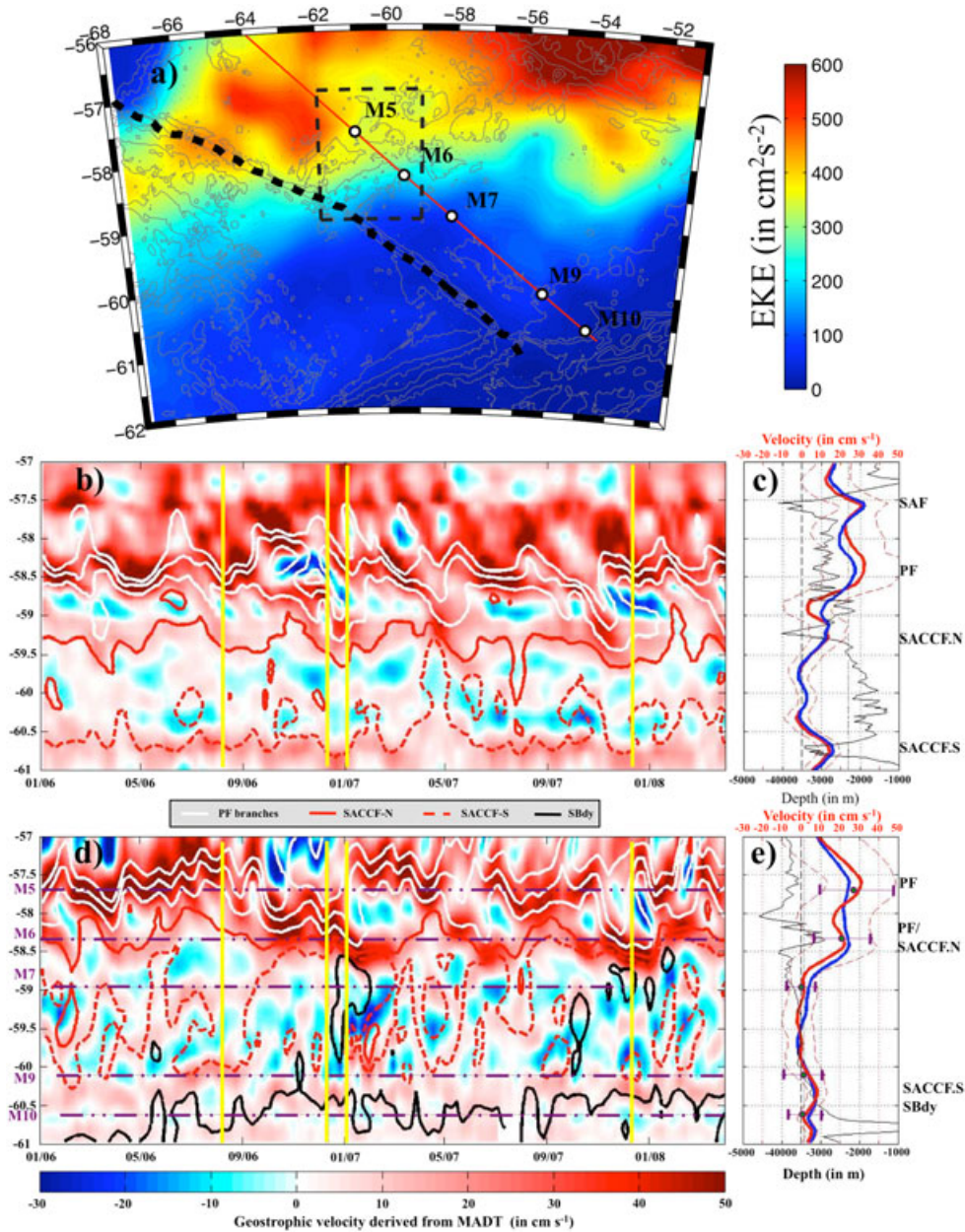


Figure 9. (a) Mean eddy kinetic energy in cm^2s^{-2} over the mooring deployment period (25 January 2006 to 1 April 2008). Mooring locations are indicated by white dots. The 4000 m and the 2000 m isobaths are shown by thin grey lines. Cross-track velocities along the dotted black line (crest of the SFZ) and the red line (track 104) are shown in Figures 9b and 9d. The black dotted square around M5 and M6 delimits the area studied in section 5.3. (b) Surface geostrophic velocities perpendicular to the crest of the SFZ and derived from MADT data during the deployment period and between 57°S and 61°S . Velocities are in centimeters per second (cm s^{-1}). Solid yellow lines mark the dates of the situations shown in Figure 2 and Figure 10. Locations of PF branches are shown in white, SACCF branches in red and SBdy front in black. (c) The red solid line corresponds to the mean across-track surface velocity during the mooring period and the red dotted line to the standard deviation. The black line corresponds to the bathymetry (in meters). Mean across-track surface velocity over the 1992–2010 period is represented by the blue line. Figures 9d and 9e are analogous to Figures 9b and 9c for track 104. (d) Dash-dotted horizontal violet lines indicate the mooring locations and record length. (e) The mean and standard deviation of the across-track component of the in situ velocity at the upper current meter are shown in violet.

5.1. Cross-Track Velocities Along Jason Tracks 28 and 104

[36] At the entrance to the Ona Basin, local maxima in mean cross-track velocities corresponded to depressions or gaps in the Shackleton transverse ridge (Figures 9b and 9c). The SACCF-S flowed through the Shackleton Gap (60.7°S and 3700 m depth) with a mean velocity of 0.15 m s^{-1} . The mean velocity associated with the SACCF-N had the same value (0.15 m s^{-1}) and was found at 59.2°S over a 4000 m deep gap in the ridge (Figure 9c). The crest of the ridge between the mean SACCF-N and SACCF-S locations is less than 2000 m below the sea surface. Farther north, mean cross-track velocities larger than 0.3 m s^{-1} between 58.2°S and 58.6°S above depths ranging from 2500 to 3500 m corresponded to the mean location of the rejoined PF branches. The local maximum in mean cross-track velocity (0.3 m s^{-1}) at 57.6°S over another gap (deeper than 4000 m) is in the Yaghan Basin and corresponded to the flow of the SAF. The 18 year long cross-track mean velocity profile (Figure 9c, in blue) was similar to the 2 year mean profile; the only difference concerns the PF location, which was on average in a northern position during the years 2006–2008. The Shackleton Ridge is a strong constraint on the SACCF, because it causes the branches to proceed through gaps separated by 300 km. The elevation of the crest between these two gaps (less than 2000 m from the sea surface) shelters the center of the Ona Basin from the strong eastward flow of the ACC.

[37] Along track 104, three distinct regions show up in the cross-track velocity field: to the north of 58.5°S, a strong meandering eastward flow associated with the PF and the SACCF-N; between 58.5°S and 60°S, a region of weaker flow with a large amount of westward velocities; and to the south of 60°S, a region with mostly moderate eastward flow (Figure 9e). Mean cross-track velocities derived from MADT were in remarkable agreement with the means from in situ data at all moorings (Figure 9d). The mean cross-track velocities between 59°S and 60°S were small. They were negative, i.e., westward, between 59° and 59.5°S. Standard deviations of the MADT-derived cross-track velocities agreed with the standard deviation of the cross-track in situ velocities, except at the southernmost mooring where they were smaller, as already discussed in section 4.1 (Figure 9e).

[38] Most of the time along track 104, the PF branches were close to each other and were located to the north of the WSR, as suggested by the mean velocities (Figure 9d). M5, with a mean cross-track velocity close to 0.3 m s^{-1} , is thus embedded in the flow associated with the PF. The maximum cross-track velocities were obtained with M5 sampling the core of the PF (e.g., over 0.5 m s^{-1} in April–May 2006, April 2007, July 2007, November 2007, and February 2008) (Figure 9e). Large velocities were recorded when M6 was sampling either SACCF-N velocities (0.4 m s^{-1} in February 2006 and April 2006 in Figures 8a and 9d) or PF velocities (over 0.60 m s^{-1} ; e.g., January 2007, December 2007 in Figures 8a and 9d). The circulation north of 59°S is further examined in section 5.3. Altimetry showed that the PF location was on average in a northern position during the years 2006–2008 [Barré *et al.*, 2008, Figure 15a]. This northern position is reflected in the cross-track mean velocity profiles (Figure 9e) and in the observations along Jason track 28 described above.

[39] In the southern part of the Ona Basin, the maximum mean cross-track velocity associated with the SACCF-S was located at 60.25°S, to the south of the M9 location (Figure 9d). The mean velocity at M9 at 1000 m was 0.1 m s^{-1} to the northwest (Figure 5), roughly parallel to the track. On average, M9 sampled the northwestward flow associated with a SACCF-S meander (as in Figure 2). The SACCF-S meanders over the rather flat central Ona Basin and sheds eddies to the north. We cannot comment on the velocities south of 60.5°S, because their variations were largely underestimated (section 4.1). However, we noticed that the southern boundary of the ACC (SBdy) sheds eddies to the north as far north as 58°S (see next section). Mooring M7 sampled some of these eddies coming from south of the SBdy. The meandering and/or eddy-shedding of both the SACCF-S and the SBdy were particularly active after October 2006 and are discussed in the next section.

5.2. The Central Ona Basin

[40] Three MADT maps illustrating different situations in the Ona Basin are presented in Figure 10. The first map (9 August 2006) corresponds to a PF/SACCF-N located quite far north on track 104, to an SACCF-S and SBdy far to the south, and to a rather quiescent flow in the central Ona Basin (Figure 10a). Two cyclones and one anticyclone were observed between the two SACCF branches. The second map (3 January 2007) exhibits a large cyclonic ring, which occupies most of the Ona Basin (Figure 10b). The ring is centered on the M7 location where small velocities were recorded at the time. The ring detached from the developing SACCF-S meander present in the December 2006 map introduced in section 1 (Figure 2). The PF branches were in a southern position and the PF-S forms the southern boundary of an energetic anticyclonic eddy standing over the Ona seafloor depression (54°W, 58°S). On 12 December 2007 (Figure 10c), a strong cyclone was located over M7 where recorded velocities at 2415 m depth reached 0.35 m s^{-1} . Altimetric maps prior to those in Figures 10b and 10c, show small cyclones shed from the SBdy advected northwestward as far as 58°S. This advection to the northwest is possible in the shelter from the general eastward flow of the ACC provided by the SFZ. The 18 year long altimetric time series shows that the northwestward advection of water from south of the SBdy is recurrent (Figure 11). However, the SBdy reaches as far north as 59°S only on eight occasions in 18 years and the two events discussed above (Figures 10b and 10c) were of outstanding duration: they lasted several months (Figure 11). Warm-core eddies also cross track 104 recurrently (Figure 11).

5.3. Polar Front and SACCF-N Over the West Scotia Ridge

[41] We examined how the flow deflected to the north by the high southern part of the SFZ goes through the complex topography at the intersection of the SFZ with the West Scotia Ridge and subsequently over the double seamount chains of the WSR. For that, we made use of moorings M5 and M6, both being located on the flank of deep channels transverse to the main central valley of the WSR (Figures 1b and 12e). M5 data were analyzed in Ferrari *et al.* [part I, 2012]. An EOF analysis of the combined velocity data of moorings M5 and M6 provided the covarying modes at those

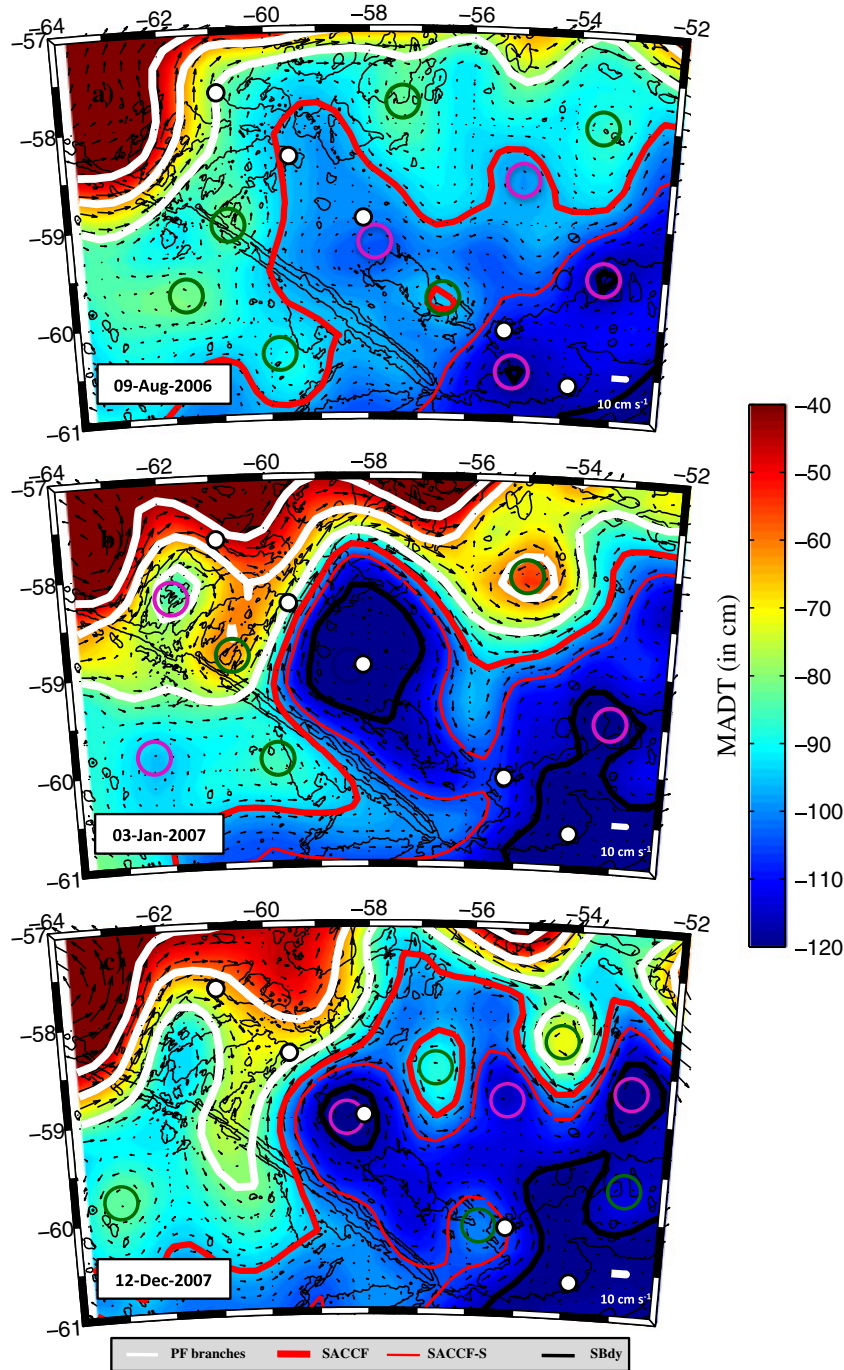


Figure 10. MADT corresponding to different dates in the Ona Basin on (a) 9 August 2006, (b) 3 January 2007, and (c) 12 December 2007. Green and violet circles mark anticyclonic and cyclonic eddies, respectively. Locations of PF branches are in white, SACCF branches in red and the SBdy front is represented by the black lines. Mooring locations are indicated by white dots.

two sites. The first three EOFs explained 81% of the total variance and were surface intensified (Figure 12a). Each EOFs showed roughly similar direction in the vertical, with an anticlockwise rotation from deep to shallow at M5 in all EOFs and clockwise rotation in EOF1 at M6. Each EOF had a different direction at M5 and M6. To gain an understanding of these modes, an EOF analysis of the SLA was performed over a small box centered on the mooring locations (62°W – 59°W and 57°S – 59°S). The box was chosen in

order to avoid the large eddy kinetic energy region to the West (Figures 12f, 12g, and 12h). The first three EOFs explained 72% of the total variance (EOF1 38%, EOF2 18%, EOF3 16%, respectively). The corresponding component of the upper level of the joint M5 + M6 EOFs were plotted on the SLA EOF component and corresponded in direction and strength to the altimetrically derived surface geostrophic velocity anomalies at the mooring points (Figures 12f, 12g, and 12h). The time series associated with

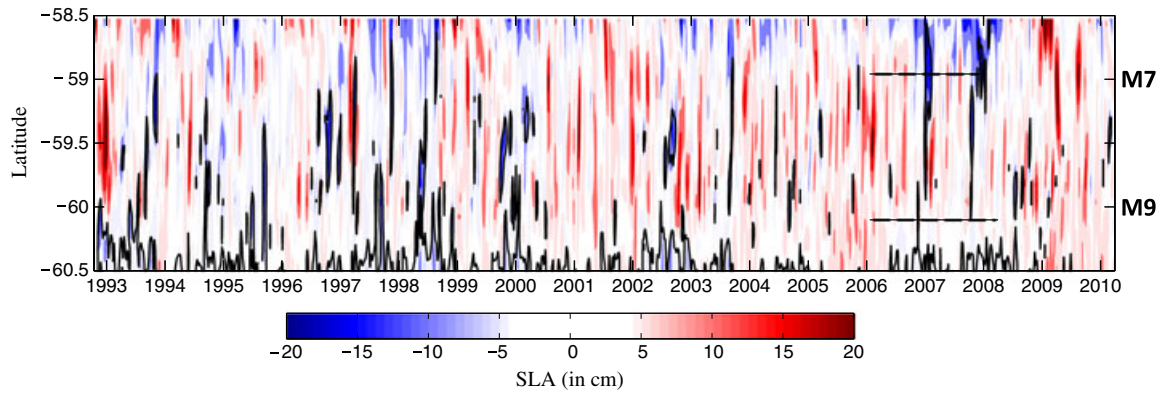


Figure 11. Time series of SLA (in centimeters) between 58°S and 60.5°S along Jason track 104 in Drake Passage. Location of the absolute dynamic topography value (−117 cm) corresponding to the SBdy front is in black.

the EOF of the two data sets bear a striking resemblance, the SLA EOF time series being smoother, as expected (Figures 12i, 12j, and 12k). The spatial structures of the SLA EOFs are obviously related to the underlying bathymetric structure, with strong flows channeled in the deep valleys and weaker flow over seamounts. Six dates, corresponding to extreme values of the three SLA EOF time series, were selected to illustrate the frontal paths associated with each EOF. The frontal branch locations were determined from the MADT gradients, as in *Barré et al.* [2011] (Figure 12).

[42] The EOF1 structure (Figure 12f) corresponded to an increase in the flow in the central valley of the WSR and a deceleration of the flow to the north of the WSR. The corresponding flows at M5 and M6 were opposite to each other and converged to feed the central valley. Indeed, the positive phase of the first mode, as illustrated on 15 November 2006, corresponded to PF branches being adjacent and flowing through the central deep valley of the WSR (Figure 13a). In the negative phase of EOF 1, e.g., 21 March 2007, the PF branches were adjacent and found to the north of the WSR at least until 58°W (Figure 13b). The SACCF-N crossed the SFZ through a depression at 59.2°S and flowed along the southern flank of the WSR. The EOF2 structure (Figure 12g) corresponded to a vortex centered on the southern side of the WSR. M5 and M6 were located on the boundaries of that vortex and the velocities at M5 and M6 were roughly perpendicular to each other. The positive phase of the second EOF, as seen on 23 May 2007, corresponded to the PF branches being separated; the northern branch of the PF (PF-N) flowing on the northward flank of the WSR, while the middle and southern branches (PF-M and PF-S) meandered over the WSR (Figure 13c). The SACCF-N joined the PF-S and entered the WSR central valley at 59°W. In the negative phase of the second EOF, as illustrated by the MADT on 22 August 2007, the PF-M branch looped to the north of the WSR and entered the deep valley at 58°W and proceeded eastward, adjacent to other PF branches, through the deep central valley of the WSR (Figure 12d). In the positive phase of the third EOF, e.g., 18 April 2007, the PF branches were separate as they crossed the SFZ. The PF-N remained to the north of the WSR, while the PF-M and PF-S meandered over the WSR (Figure 12e). The SACCF-N meandered through the deep transverse channel where M6 is located. In the negative phase

of EOF 3, the two PF branches (PF-N and PF-M) joined and made two extremely sharp meanders flowing through the transverse valleys (Figure 12g). The PF-S and SACCF-S remained on the southern side of the WSR. A small cyclonic eddy was observed near M5 location between the PF-S and the PF-M

[43] These structures observed during the 2 year mooring deployment are not anecdotal, as an EOF analysis performed over 18 years of altimetry (1993–2010) provided the same first three EOF structures explaining 68% of the total variance (not shown). EOF1 (35%) over the long period was similar to the EOF1 (38%) of the mooring period, whereas EOF2 (21%) over the long period was similar to EOF3 (18%) of the mooring period, and EOF 3 (12%) was similar to EOF2 (29%) of the mooring period. The 18 year time series indicated that EOF3 became more frequent after 2002. The 18 year long time series associated with each EOF have significant energy at time scales of two to four months. Intermittently, EOF1 also shows some energy at a lower frequency: an annual cycle was present from 2006 to 2008 at the time of the mooring deployment.

6. Summary and Discussion

[44] More than 2 years of current meter data, from January 2006 to April 2008, at four mooring sites across the Ona Basin, have been analyzed. These data are the first in situ velocity time series in the Ona Basin. Altimetrically derived surface geostrophic velocities were compared to the upper level in situ velocity data. Having shown that the altimetrically derived velocities were consistent with the in situ data, we used the altimetry to further describe the circulation in the Ona Basin, to interpret the observations at the isolated mooring sites and to put them in the context of the 18 year long altimetry time series. We recall here the major results and draw the corresponding conclusions.

[45] 1. Variability was isotropic, with variance ellipses being close to circular except on the southernmost mooring over the continental slope where variability was amplified in the direction of the isobaths. The variability was coherent in the vertical, similarly to that observed on the other side of the SFZ by the DRAKE 79 data analyzed by *Inoue* [1985]. Therefore altimetry was potentially a useful tool to monitor velocity variations and comparisons were performed.

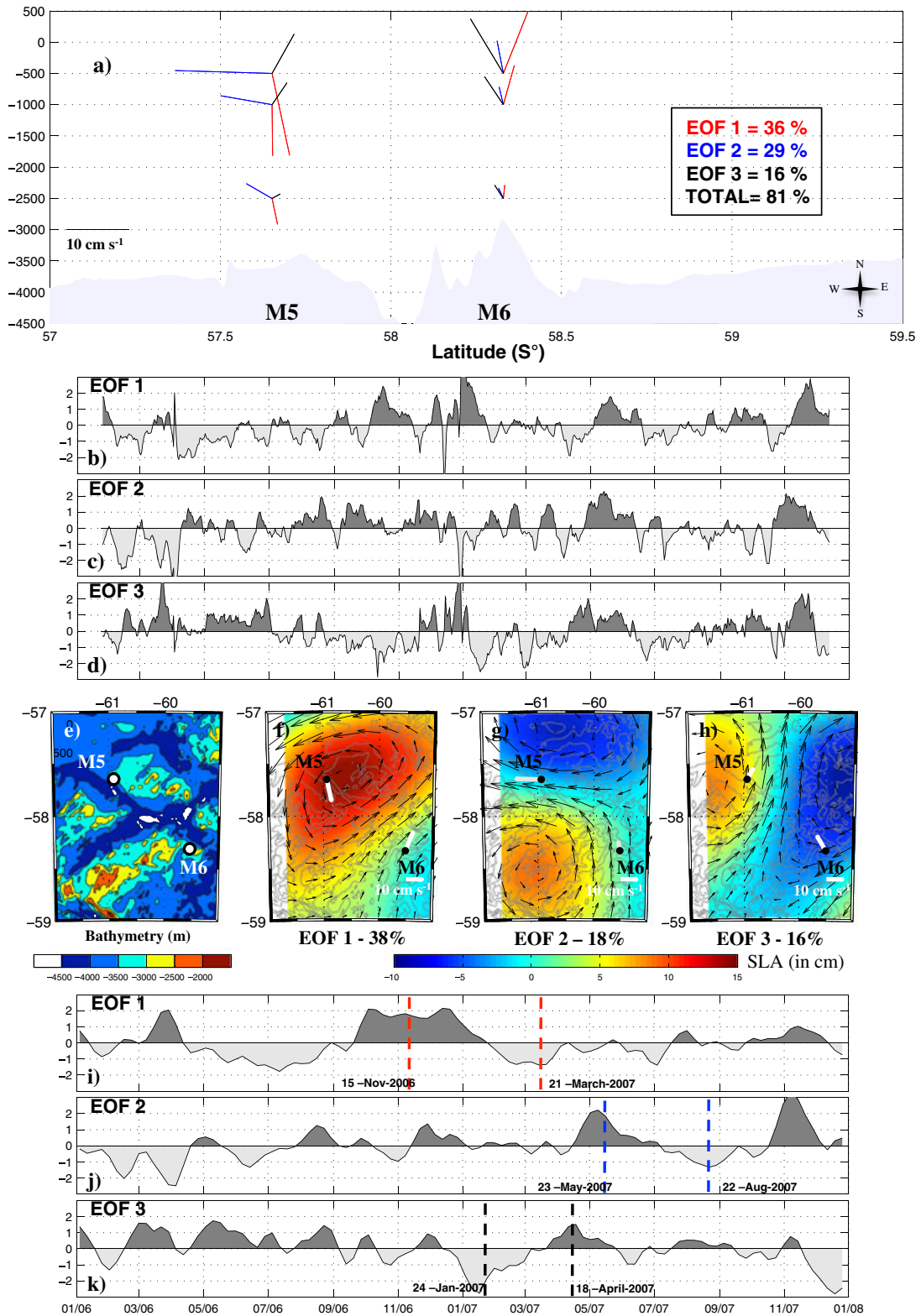


Figure 12. EOF analyses of moorings and SLA over the WSR (57°–59°S, 59°–62°W). (a) Joint EOFs for moorings M5 and M6. The first, second and third modes are represented in red, blue and black, respectively. (b, c, d) Time series associated with the EOFs shown in Figure 12a. (e) Locations of moorings M5 and M6 and sea-floor topography (in meters). (f) First, (g) second, and (h) third EOFs of SLA (in centimeters). Black arrows represent the geostrophic velocity anomaly vectors. White arrows represent the mooring EOF components at 500 m depth from Figure 12a. (i, j, k) Time series associated with EOFs of SLA. Dashed red, blue, and black vertical lines mark dates of positive and negative phases of EOF 1, 2, and 3, respectively.

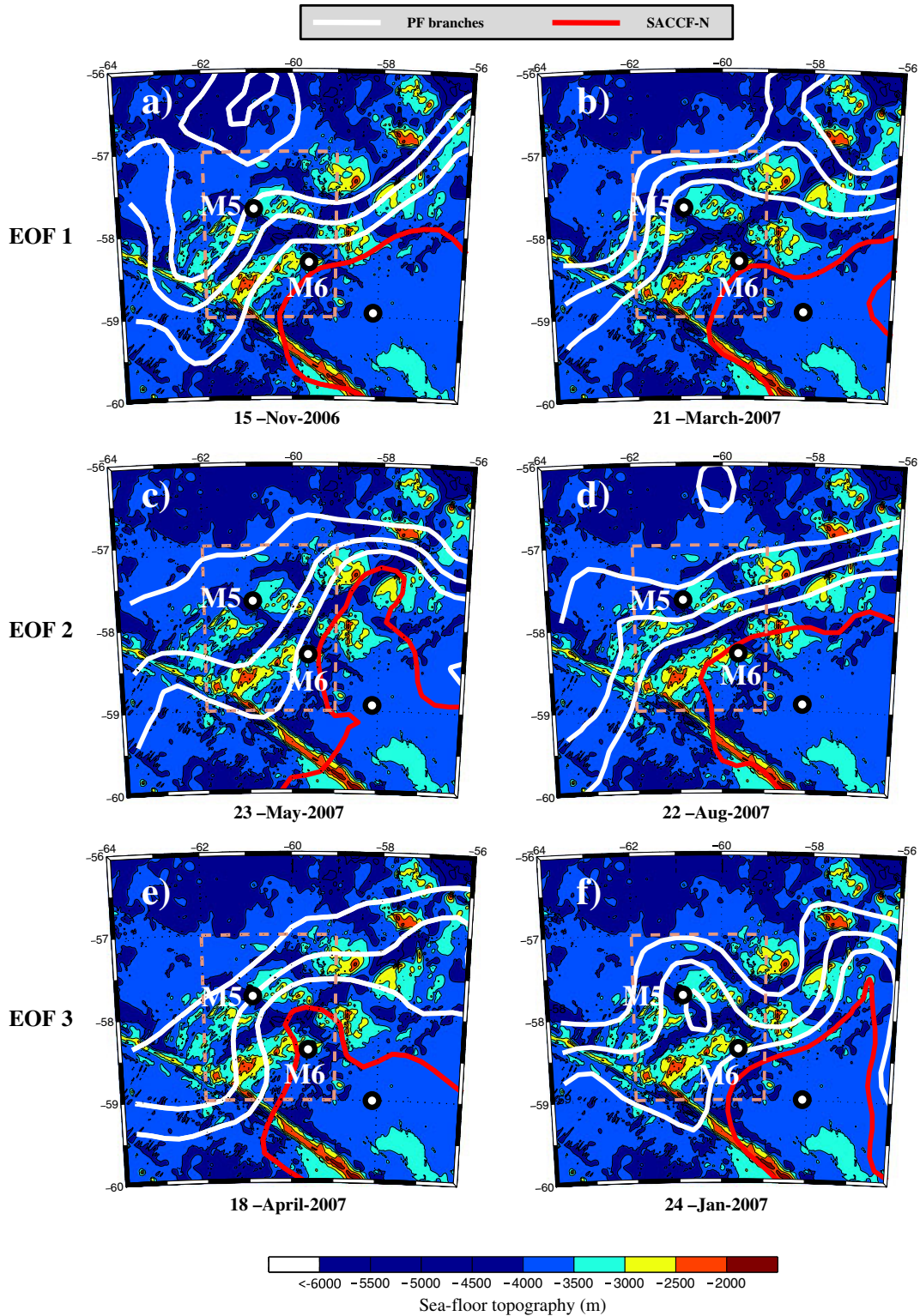


Figure 13. Locations of the frontal branches over the WSR sea-floor topography at the dates selected in Figures 12i, 12j, and 12k representative of a negative or a positive phase of each EOF. Locations of the PF branches are in white and location of the SACCF-N branch is red.

[46] 2. The 7 day multisatellite gridded maps of absolute dynamic topography provided surface geostrophic velocities that were in satisfactory agreement with the in situ velocities at M6 and M7 (means, standard deviations, correlations). However, the averaging used to produce the

maps led to a significantly smaller velocity variance than the in situ velocity variance for the two southernmost moorings. At M9, MADT-derived geostrophic velocities, although underestimated in amplitude, satisfactorily described the temporal variations of the in situ velocity. At M10, in situ

and MADT-derived cross-track velocities were uncorrelated. Significant correlations (99% level) were obtained at M10 when using the CTOH altimetry product. Work is ongoing to develop an appropriate data treatment for the southern part of the Ona Basin.

[47] In spite of these limitations in the south, MADT were most useful in describing the circulation in the Ona Basin and interpreting the in situ measurements.

[48] 1. First of all, a section of MADT-derived velocity across the crest of the Shackleton Ridge at the western entrance to the Ona Basin showed that deep gaps in the ridge control the mean location of the ACC frontal branches (section 5.1). In particular, the two SACCF branches went through two gaps that are 300 km apart. The crest of the ridge, less than 2000 m below the sea surface between those two gaps, provides a relative shelter from the eastward flow of the ACC.

[49] 2. The mean velocities observed at the mooring sites were consistent with a mean cyclonic circulation in the Ona Basin, as described from altimetry by *Barré et al.* [2008] and *Provost et al.* [2011]. Mean velocities were larger than their standard deviation at two mooring sites: at mooring M6, which recorded the strong eastward flow associated with the PF and SACCF-N over the WSR, and at mooring M9, which sampled a northwestward flow associated with the SACCF-S overshoot to the north right after proceeding through the Shackleton Gap. Velocity variance ellipses for the central Ona Basin were close to circular and stretched in the direction of the isobaths over the continental slope (M10, 60.5°S).

[50] 3. In the complex area where the SFZ intersects the WSR, the MADT maps provided an accurate documentation of the meandering of the PF branches around the seamounts, in remarkable agreement with the current meter data.

[51] 4. Altimetric data also helped in the interpretation of the mean downwelling indicated by a counterclockwise rotation of the mean velocity vectors at M6 and M9, and of the mean upwelling suggested by a clockwise rotation of the mean velocity vector at M7 and M10. Indeed, upwelling and downwelling may reflect the dominant mesoscale activity at the moorings located in a flat region, namely M7 and M9. As shown by altimetry, there is preferential cyclonic activity at M7, and preferential anticyclonic eddies at M9 (Figure 11). The mean upwelling at M10 was consistent with the mean direction of the flow at depth in terms of the bottom topography (Figure 5) and with a preferential cyclonic meandering and cyclonic-eddy-shedding there [*Provost et al.*, 2011]. The downwelling observed at depth at M6 may be explained by M6's location downstream of a major ridge.

[52] 5. Altimetry helped to put the mooring period into perspective and in particular to show that some of the events sampled during the mooring period were exceptional, such as the invasions of water from south of the SBdy over a large part of the Ona Basin (Figures 10b and 10c). An active ventilation of the Circumpolar Deep Water by water from the south of the SBdy was shown to be associated with cyclonic eddies and their filaments [*Provost et al.*, 2011]. Such exceptional events, filling the whole Ona Basin with water from south of the SBdy, as described in section 5.2, are of another dimension. The circumstances that led to those events need to be examined.

[53] Time series of temperature and salinity acquired on these moorings are being used to compute mean and eddy fluxes and will be presented soon. The detailed examination of the currents performed herein is a prerequisite for the interpretation of the fluxes and putting them into perspective.

[54] Last but not least, the satisfactory comparison with altimetrically derived surface velocities and the vertical coherence of the horizontal velocity revealed by the current meter data are encouraging in terms of the computation of the volume transport using the method applied to the Malvinas Current by *Spadone and Provost* [2009].

Appendix A: Mean Vertical Velocity

[55] A simple steady state theory of the geostrophic velocity field, the beta spiral, predicts the existence of current spirals associated with either the vertical component of velocity or local density changes due to heating or cooling [*Bryden*, 1976; *Schott and Stommel*, 1978]. The formula linking the rotation of the mean current vector to the velocity is

$$\theta_z = -\frac{g}{f\rho_0|u|^2}(w\rho_z - \dot{\rho}) \quad (\text{A1})$$

where θ is the direction angle of the horizontal velocity u , measured anticlockwise in radians, $\dot{\rho}$ is the density increase by local in situ source of cooling, f the Coriolis parameter, g the gravity, ρ_z the density variation with increasing depth, ρ_0 the mean potential density and w the mean vertical velocity.

[56] If we neglect in situ source of cooling, the equation reduces to

$$\theta_z = -\frac{N^2 w}{f|u|^2} \quad (\text{A2})$$

where N is the Brunt-Vaisälä frequency $N^2 = -(\partial\rho/\partial z)$

[57] Therefore, the sense of rotation of the horizontal mean velocity vector with increasing depth is anticyclonic where the vertical velocity is downward and it is cyclonic where the vertical velocity is upward.

[58] We estimated mean vertical velocities (w) from the data using

$$w = -\frac{\theta_z f |u|^2}{N^2} \quad (\text{A3})$$

[59] We produced several estimates of w (Table A1) using the angle difference between successive mean velocity vectors on the vertical ($\theta_z = (\theta_{i+1} - \theta_i)/(z_{i+1} - z_i)$), the horizontal mean velocity amplitudes u_i at the current meter level i and several estimates of the Brunt-Vaisälä frequency from the hydrographic data of the deployment and recovery cruises. This way we produced nine estimates of w at each mooring using three different estimates for N^2 (from deployment and recovery cruises) and three different values for u (u estimated at each current meter level and a mean u) (Table A1). Vertical velocity amplitude estimates varied from 0.2 to 28.6 meters per day. From these different estimates we produced a mean velocity, a standard deviation and noted the minimum and maximum values (Table A1). The means were on the order of a few to ten meters per day and larger than the standard deviation in most cases.

[60] Neglecting in situ cooling is a suitable approximation at these intermediate and deep depths, even in winter at this latitude.

Table A1. Mean Vertical Velocity Estimates in m day^{-1} . Negative Velocity Corresponds to Downwelling and Positive Velocity to Upwelling

| Mooring | M6 | | M7 | | M9 | | M10I | | M10II | | M10III | |
|-----------------|-------------|--------------|-------------|--------------|----|---------------|--------------|---------------|--------------|---------------|--------------|---------------|
| Depth in meters | 237/ 828 | 828/ 2449 | 467/ 991 | 991/ 2553 | - | 1057/ 2560 | 500/ 1000 | 1000/ 2500 | 500/ 1000 | 1000/ 2500 | 500/ 1000 | 1000/ 2500 |
| Mean | -9.3 | -17.3 | 3.8 | 2.0 | - | -15.1 | 1.5 | 4.0 | - | 2.4 | 0.7 | - |
| σ | 5.1 | 5.3 | 4.2 | 1.6 | - | 5.9 | 0.3 | 2.7 | - | 2.7 | 0.1 | - |
| Min. | -4.0 | -10.6 | 0.2 | 0.3 | - | -8.1 | 1.2 | 1.6 | - | 0.3 | 0.7 | - |
| Max. | -19.6 | -28.6 | 12.6 | 4.8 | - | -27.1 | 1.8 | 7.0 | - | 5.5 | 0.8 | - |

[61] **Acknowledgments.** We are deeply grateful to the captains and crews of the R/V *Polarstern* for their help and for creating excellent work conditions during the DRAKE cruises, and to Eberhard Fahrbach (AWI) for his support. Financial support was provided both by the CNES (Centre National d'Etudes Spatiales) and by CNRS-INSU (Institut des Sciences de l'Univers) through the LEFE/IDAO program. J.H. Lee was supported by the Korea Meteorological Administration Research and Development Program under Grant CATER 2008-4209. R. Ferrari acknowledges an INEE (Institut National de l'Environnement et de l'Ecologie) Ph.D. scholarship. We also thank Ray C. Griffiths for his valuable comments on the manuscript.

References

Barré, N., C. Provost, N. Sennéchael, and J. H. Lee (2008), Circulation in the Ona Basin, southern Drake Passage, *J. Geophys. Res.*, *113*, C04033, doi:10.1029/2007JC004549.

Barré, N., C. Provost, A. Renault, and N. Sennéchael (2011), Mesoscale activity in Drake Passage during the cruise survey ANT-XXIII/3: a satellite perspective, *Deep-Sea Res., Part II*, doi:10.1016/j.dsr2.2011.01.003.

Bryden, H.L. (1976), Horizontal advection of temperature for low-frequency motions, *Deep-Sea Res.* *23*, 1165–1174.

Cronin, M., K. L. Tracey, and D. R. Watts (1992), Mooring motion correction of the SYNOP Central Array current meter data, *GSO Tech. Rep.* 92-4, University of Rhode Island, 114 pp.(http://www.po.gso.uri.edu/dynamics/publications/tech_rpts/tech_rpt_92-4.pdf).

Cunningham, S. A., S. G. Alderson, B. A. King, and M. A. Brandon (2003), Transport and variability of the Antarctic Circumpolar Current in Drake Passage, *J. Geophys. Res.*, *108*(C5), 8084, doi:10.1029/2001JC001147.

Ducet, N., P.-Y. Le Traon, and G. Reverdin (2000), Global high resolution mapping of ocean circulation from TOPEX/Poseidon and ERS-1/2, *J. Geophys. Res.*, *105*, 19,477–19,498.

Ferrari, R., C. Provost, A. Renault, N. Barré, N. Sennéchael, Y.-H. Park, J.-H. Lee (2012), Circulation in Drake Passage revisited using new current time series and satellite altimetry: 1. The Yaghan Basin, *J. Geophys. Res.*, *117*, C12, doi:10.1029/2012JC008264.

Hofmann, E.E. and T. Whitworth, 1985. A synoptic description of the flow at Drake Passage from year-long measurements. *J. Geophys. Res.*, *90*, 7177–7187.

Hogg, N. G. (1986), On the correction of temperature and velocity time series for mooring motion, *J. Atmos. Oceanic Technol.*, *3*, 204–214.

Hogg, N. G. (1991), Mooring motion corrections revisited, *J. Atmos. Oceanic Technol.*, *8*, 289–295.

Inoue, M., 1985. Modal decomposition of low frequency currents and baroclinic instability at Drake Passage. *J. Phys. Oceanogr.*, *15*, 1157–1181.

Kahru, M., B. G. Mitchell, S. T. Gille, C. D. Hewes, and O. Holm-Hansen (2007), Eddies enhance biological production in the Weddell-Scotia Confluence of the Southern Ocean, *Geophys. Res. Lett.*, *34*, L14603, doi:10.1029/2007GL030430.

Kartavtseff, A. (2008), Mouillages Drake, Courantomètres – Profileurs – Capteurs P,T,C, POLARSTERN, Janvier 2006–Avril 2008. *Rapport Interne LOCEAN*, Université Pierre et Marie Curie, 321 pp. (Available from LOCEAN, BC 100, 4 place Jussieu, 75005 Paris, France).

Lee, J. H., S. T. Jang, C. S. Hwang, and C. Provost (2007), Observation of deep currents in the southern Drake Passage, *Geophys. Res. Abstr.*, *EGU General Assembly 2007*, *9*, 0454.

Orsi, A., T. Whitworth, and W. Nowlin (1995), On the meridional extent and fronts of the Antarctic Circumpolar Current, *Deep-Sea Res., Part I*, *42*, 641 – 673, doi:10.1016/0967-0637(95)00021-W.

Provost, C., A. Renault, N. Barré, N. Sennéchael, V. Garçon, J. Sudre, and O. Huhn (2011), Two repeat crossings of Drake Passage in austral summer 2006: Short-term variations and evidence for considerable ventilation of intermediate and deep waters, *Deep-Sea Res. II*, doi:10.1016/j.dsr2.2011.06.009.

Renault, A., C. Provost, N. Sennéchael, N. Barré, and A. Kartavtseff (2011), Two full-depth velocity sections in the Drake Passage in 2006 – Transport estimates, *Deep-Sea Res., Part II*, doi: 10.1016/j.dsr2.2011.01.004.

Rio, M. H., P. Schaeffer, G. Moreaux, J. M. Lemoine, and E. Bronner (2009), A new mean dynamic topography computed over the global ocean from GRACE data, altimetry and in-situ measurements, poster presented at OceanObs'09 Conference, European Space Agency, Venice, Italy, 21–25 Sept 2009.

Roblou, L., F. Lyard, M. Le Henaff, and C. Maraldi (2007), X-track, a new processing tool for altimetry in coastal oceans, *Geoscience and Remote Sensing Symposium*, IGARSS 2007, IEEE International 23–28 July 2007, page(s):5129–5133, doi: 10.1109/IGARSS.2007.4424016.

Schott F. and H. Stommel (1978), Beta spirals and absolute velocities in different oceans. *Deep Sea Res.*, *25*, 961–1010.

Sokolov, S., and S. R. Rintoul (2009), Circumpolar structure and distribution of the Antarctic Circumpolar Current fronts: 1. Mean circumpolar paths, *J. Geophys. Res.*, *114*, C11018, doi:10.1029/2008JC005108.

Spadone, A., and C. Provost (2009), Variations in the Malvinas Current volume transport since October 1992, *J. Geophys. Res.*, *114*, C02002, doi:10.1029/2008JC004882.

Spreen, G., L. Kaleschke, and G. Heygster (2008), Sea ice remote sensing using AMSR-E 89-GHz channels, *J. Geophys. Res.*, *113*, C02S03, doi:10.1029/2005JC003384.